Chapter 7

Transient Photocurrent Measurements

In the previous Chapters, the density and distribution of defects as well as band-tail states in μc-Si:H were studied. The presence of these localized states strongly influences the charge carrier transport in the material. Time resolved charge transport measurements are a powerful tool, which have been successfully applied to e.g. a-Si:H [97] to study charge transport mechanisms and electronic states associated with the transport. In μc-Si:H there is, of course, a wide range of possible structure compositions giving rise to the possibility that transport properties may also vary considerably. In this section, a study of hole drift mobility measurements performed on material prepared under conditions for optimum solar cell performance will be presented. Various samples, as listed in table 7.1, have been prepared as described in section 3.3.2 and charge carrier transport has been investigated by time-of-flight experiments. The specimens can be divided into two groups. While for samples C and D the depletion width d_w extends over the entire i-layer thickness d_i, for samples A and B this is not the case.

7.1 Electric Field Distribution

The standard time-of-flight analysis requires a uniform distribution of the externally applied field within the specimen. The method relies on the fact, that a typical time-of-flight sample acts as a capacitor, thus Eq. 3.13 applies. Ideally, the film is fully depleted and the depletion layer d_w extends over the entire sample thickness d_i, indicating a uniformly distributed electric field within the specimen. While this behavior is typically observed for a-Si:H diodes, capacitance measurements performed on microcrystalline silicon diodes suggest that in μc-Si:H this is not always the case [143, 144].

Table 7.1: Properties of microcrystalline silicon *pin* diodes used in the TOF experiment. Listed are the Raman intensity ratio I_C^{RS}, the i-layer thickness d_i, the depletion width d_w, the capacitance C(4V,300K), and C_{geom} calculated from the geometry (see section 7.1).

Sample	I_C^{RS}	d_i [μm]	d_w [μm]	C(4V,300K) [pF]	C_{geom} [pF]
A	0.71	4.0	1.3	60	20
B	0.70	6.5	1.7	46	13
C	0.60	3.4	3.4	22	22
D	0.61	4.3	4.3	18	18

Depletion Layer Capacitance

Capacitance measurements have been performed on samples A-D (see table 7.1) for different applied voltages V and varying temperatures T, as described in section 3.13. The measured values of the capacitance are plotted in Fig. 7.1. Also indicated are the geometrical values C_{geom} calculated using Eq. 3.13 with $d_w = d_i$. In Fig. 7.1 (a) the measured values of the capacitance are plotted as a function of the applied voltage, measured at a temperature of 300K. One can observe that, from the characteristic of the capacitance the specimens can be divided into groups. While for sample C and D the capacitance is independent of the applied voltage and agrees very well with the values expected from the geometrical dimensions, samples A and B significantly deviate from this behavior. For samples A and

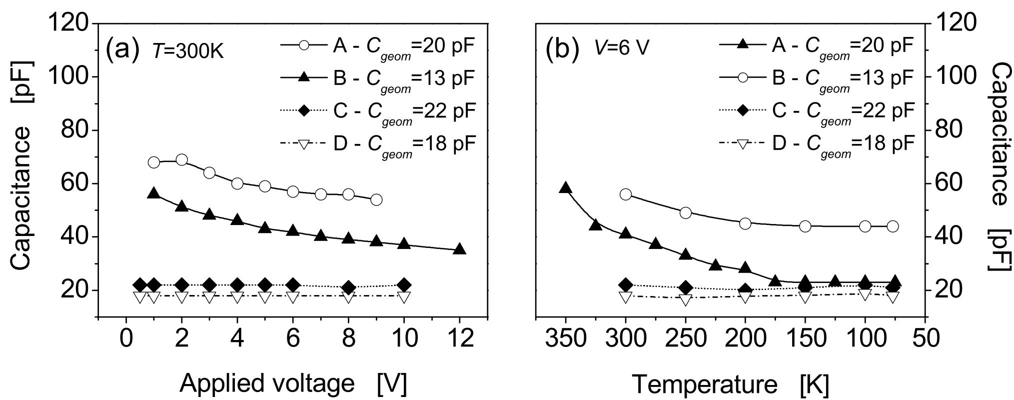

Figure 7.1: *Sample capacitance of the samples A-D versus (a) the externally applied voltage and (b) the temperature. The geometrical capacitance C_{geom} shown in the legend has been calculated using Eq. 3.13 and $d_w = d_i$.*

B the capacitance decreases with increasing specimen thickness d_i, as expected from Eq. 3.13 (see table 7.1). However, for both samples the measured values are higher than one would expect from the geometry of the structure. With increasing applied reverse voltage the capacitance decreases, indicating an increasing depletion layer width. The capacitance also decreases with decreasing temperature (see Fig. 7.1 (b)). However, even for the highest voltage of $V = 12$ V or the lowest temperature, the capacitance of samples A and B deviates considerably from C_{geom}. The excess of C indicates that the depletion width d_w (see table 7.1) does not extend over the whole sample thickness and the electric field is concentrated in only a fraction of the sample.

From the capacitance measurements the specimen investigated can be divided into two groups. For samples C and D the depletion width d_w is close to the physical layer thickness d_i. This criterion corresponds to a nearly uniform electric field across the intrinsic layer during the time-of-flight experiment. On the other hand, sample A, B do not satisfy this criterion. The shortage of the depletion width, compared to the i-layer thickness, indicates that the electric field is not uniformly distributed and rather concentrated to only a fraction of the sample.

7.2 Transient Photocurrent Measurements

Transient photocurrent measurements were applied to all samples listed in table 7.1, in order to determine the properties of the drift of holes. The first part of this section deals with the transients taken of specimens A and B. Since a detailed analysis of these transients failed due to the unknown electric field distribution, results will be discussed qualitatively only. In the second part photocurrent transients of specimens C and D are presented. As shown above, for both samples the electric field, applied during in the TOF experiment, is uniformly distributed across the i-layer and the transients could be analyzed in terms of a standard time-of-flight analysis.

7.2.1 Non-Uniform Electric Field Distribution

Although the electric field distribution within samples A and B is not uniform, which is a basic requirement for a TOF experiment to be suitable, transient photocurrent measurements were also done on these samples. In Fig. 7.2 photocurrent and photocharge transients for different applied voltages measured for specimens A and B are shown. All transient currents were taken at a temperature of 300K; the photocharge transients were determined by integrating the currents. The samples have been illuminated through the n-layer using an excitation wavelength of

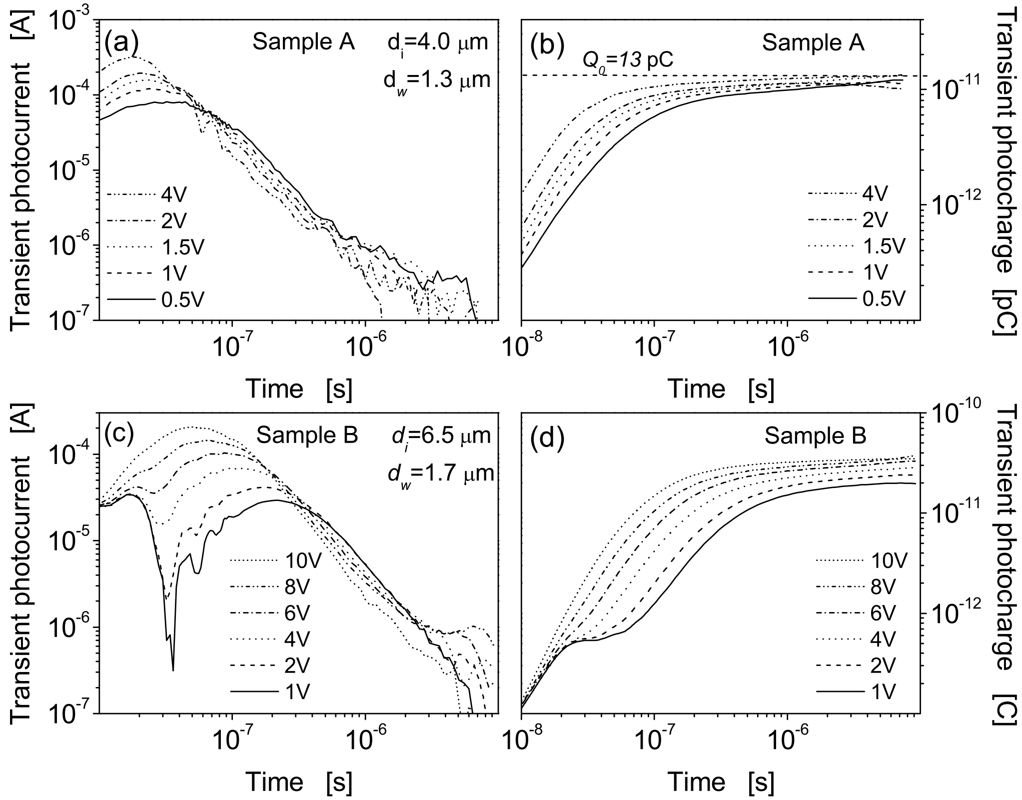

Figure 7.2: *Transient photocurrent and photocharge measured for (a, b) sample A and sample B are shown (a, b) and (c, d), respectively. The transients were taken at a temperature of T = 300K for different applied voltages at room temperature.*

λ=500 nm (E_{Photon}=2.48eV). For samples A and B with a Raman crystallinity of I_C^{RS} ~0.7 the absorption coefficient is α ≈5.5×10^4 cm^{-1}, which corresponds to an absorption depth in the intrinsic layer of about 0.16 μm [175]. While the electrons, generated very close to the n-layer, are swept away very quickly (within nanoseconds), the photogenerated holes have to traverse most of the thickness of the intrinsic layer before reaching the p-layer. Thus nearly the entire photocurrent corresponds to hole motion (see section 3.1.4 for a detailed description).

As discussed above, for both samples A and B the depletion layer width d_w is considerably lower than the real i-layer thickness d_i (see table 7.1). This indicates a nonuniform distribution of the electric field within the specimen and, therefore, unsurprisingly the transients do not show any typical shape, i.e. neither Gaussian nor dispersive transport behavior (compare section 2.3.2 and Fig. 2.4). In fact, an interpretation of the transients in terms of the properties of charge carrier transport is impossible, because of the unknown electric field distribution. However,

the transients show some interesting features which will be discussed below. In Fig. 7.2 (a) photocurrent transients of sample A are shown. Capacitance measurements have shown that the depletion layer has a width of $d_w = 1.3\ \mu$m and extends to about 1/3 of the real i-layer thickness (see table 7.1). One can observe that, after an increase of the current ($t < 2 \times 10^{-8}$ s), which is caused by the RC-constant of the measurement circuit, the current starts to decrease with a power-law in time. The decrease starts at earlier times for increasing bias voltage and a ”crossover” of the currents can be observed. The power-law decay is independent of the applied voltage and one does not observe any change in slope corresponding to a transit time, as expected for dispersive transport (compare section 2.3.2). The photocharge (panel (b)) determined by integrating the photocurrent transients approaches an asymptotic value at prolonged times, indicating that Q_0 is still a good estimate of the photoinjected charge.

On the other hand, the transits measured on sample B show a quite unexpected behavior. The photocurrent transients and the photocharge are shown in Fig. 7.2 (c, d). For this sample, the depletion layer width extends only to one fourth of the i-layer thickness. The currents shown in panel (c) show a shape that strongly depends on the applied voltage. As for early times ($t < 2 \times 10^{-8}$ s) the current is determined by the RC rise time of the measurement circuit, the current for e.g. the 1 V transient drops down to almost zero for about 80 ns before it increases again. The current peaks at about 200 ns before it starts to decrease with a power-law decay as observed for specimen A. In the photocharge transient plotted in panel (d) this effect is observable in a plateau at times between $t = 2 \times 10^{-8}$ s and 1×10^{-7} s. With increasing voltage the time range of ”zero current” becomes shorter, the effect is less pronounced and disappears for the highest voltage $V = 10$ V. The ”zero-current” and the plateau observed in the charge transients indicate that within the sample there are regions, where the energy of the externally applied field is smaller than kT and the charge carrier packet has to cross this section by diffusion. As diffusion is a statistical process no current can be observed. At the time the packet has crossed this low electric field region, the charge carrier drift can again be measured in the external circuit. With increasing applied voltage the depletion width increases and therefore the electric field penetrates deeper into the film; the effect becomes less pronounced.

Unfortunately, because of the unknown electric field distribution within the sample, the transients can not be readily analyzed to obtain drift-mobilities. Even if the field distribution were known, there are no established techniques for analyzing transients with nonuniform fields to obtain dispersive mobility parameters. The reason for the nonuniform electric field might be a high concentration of free charge carrier in this intentionally undoped material. A series of samples with different compensation levels could provide additional information [143].

7.2.2 Uniform Electric Field Distribution

Unlike samples A and B, in samples C and D the depletion layer thickness d_w extends over the whole i-layer, indicating a uniform distribution of the electric field. Fig. 7.3 (a) and (c) show photocurrent transients taken at T = 250K on specimens C and D for several applied bias voltages.

The transient photocurrents were measured for several bias voltages in the range between V=0 V and V=6 V. The transient at 0 V is due to the ”built-in” electric field, and indeed such transients have been used to infer the internal fields (see e.g. [176]). Each transient shows two power-law segments, the ”pretransit” with a fairly shallow power-law decay and the ”posttransit” regime with a steep decay. This is a signature of dispersive transport (compare section 2.3.2). The currents, obtained for different voltages, do intersect, which indicates a voltage dependent transit time t_τ. In other words, with increasing voltage the change in the power law occurs earlier, resulting in a ”crossover” of the currents. Because the time where the change in the power law occurs is interpreted as t_τ, this indicates a decreasing transit time upon increasing V. Fig. 7.3 (b, d) show the transient photocharge $Q(t,V)$ for varying externally applied voltage obtained by integrating the transient photocurrent $I(t)$ (shown in Fig. 7.3 (a, c)). The photocharge at longer times and for higher voltages approach a constant value, denoted as Q_0, which was used to estimate the total photogenerated charge. The fact, that the charge measurement for the higher voltages approach the same asymptotic value for the total charge of Q_0=25 pC and Q_0=20 pC for sample C and D, respectively, indicates that Q_0 is likely a good estimate of the charge of photogenerated holes. It seems important to note, that the difference of Q_0 between both samples is due to different laser intensities and not due to any loss of photoexcited charge carriers within the intrinsic layer. This is different for the 0 V applied voltage. Even though the photocurrent transient has the form expected for time-of-flight, it does not show the correct asymptotic photocharge. In this case holes are indeed trapped, presumably in dangling bonds, before they could reach the collecting electrode. The time required for a charge carrier to reach the collecting electrode is of the order of the deep trapping life time t_D, hence not all the photoinjected charge can be collected. In Fig. 7.4 the collected photocharge $Q(\infty)$ for sample C and D is plotted versus the externally applied voltage V. The value of $Q(\infty)$ was determined after $t = 6\times10^{-6}s$ for both samples; for higher voltages $Q(\infty)$ saturates indicating that all the photoinjected charge has been collected. Determining the photoinjected charge from the high voltage transients, the deep trapping mobility-lifetime product $\mu\tau_{h,t}$ can be evaluated using

$$\mu\tau_{h,t} = \frac{Q(\infty)}{Q_0}\frac{d_i^2}{(V+V_{int})}, \tag{7.1}$$

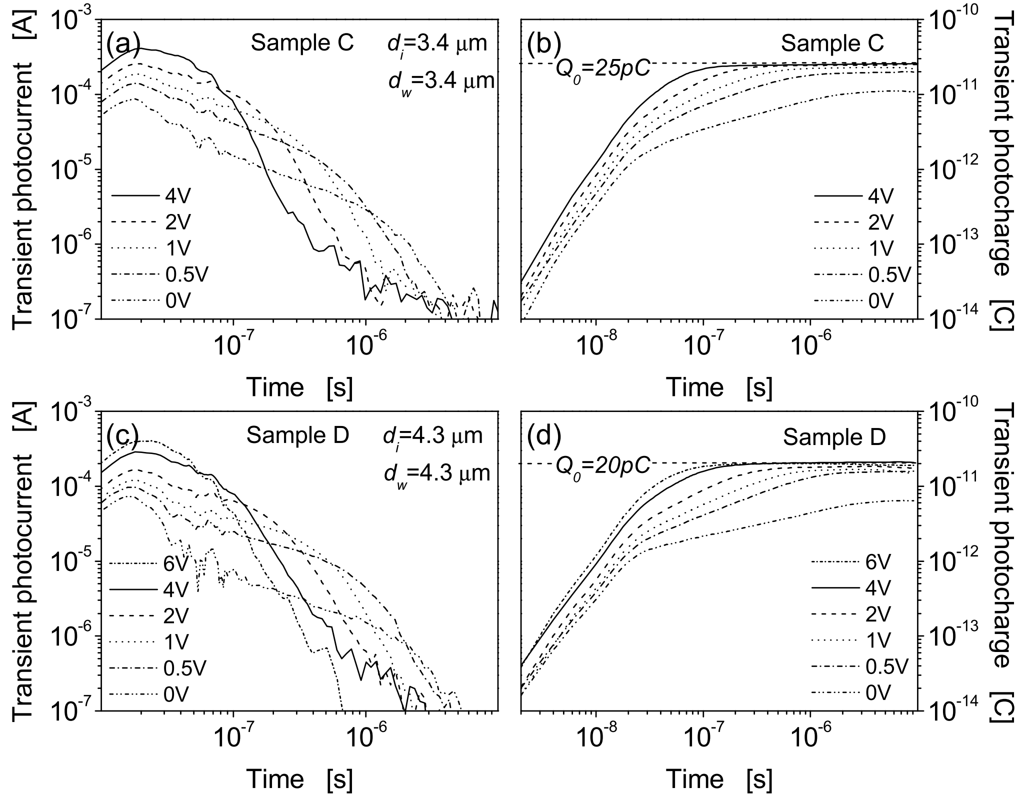

Figure 7.3: *Panel (a) and (c) show transient photocurrents taken at $T = 250K$ on specimen C and D for several applied bias voltages. The corresponding $Q(t)$ (b, d) were determined by integrating the transient photocurrent. The asymptotic value Q_0 is a measure of the photogenerated charge.*

where V is the externally applied and V_{int} the voltage due to the built-in field of the pin structure [177]. For low voltages $Q(\infty)$ increases linearly and from the slope a $\mu\tau_{h,t}$ product of $\mu\tau_{h,t} = 1 \times 10^{-7}$ cm^2/V for specimen C and $\mu\tau_{h,t} = 2 \times 10^{-7}$ cm^2/V for D can be extracted. The crossing point of this line with the x-axis is an estimate of the internal voltage V_{int} caused by the built-in field of the pin-structure, which amounts to $V_{int} = 0.4$ V for specimen C and $V_{int} = 0.3$ V for specimen D. This analysis assumes that the internal field is uniform for an external voltage of V=0 V. Evidence for this assumption comes from the normalized photocurrents discussed below.

For Fig. 7.5 the transient photocurrents of Fig. 7.3 were normalized using $I_{norm} = I(t)d_i^2/(Q_0(V+V_{int}))$. Q_0 is the total charge generated in the structure, d_i is the i-layer thickness, V is the externally applied voltage, and V_{int} is the correction for the built-in field. This normalization procedure eliminates the simple Ohmic

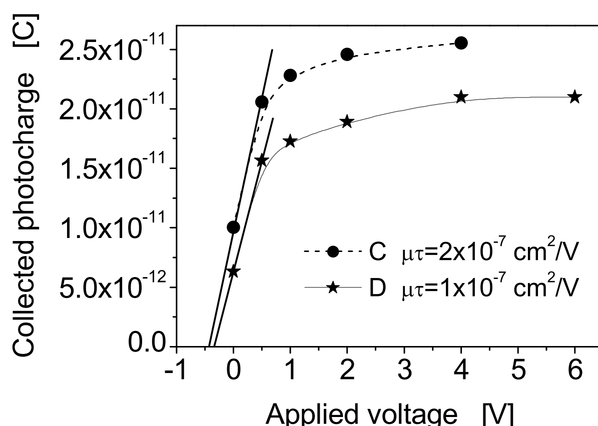

Figure 7.4: *Total photocharge $Q(\infty)$ of holes collected after $t = 6 \times 10^{-6} s$ as a function of applied voltage ("Hecht Plot"). The data points were taken from Fig. 7.3 (b) and (d).*

scaling of $I(t)$ prior the transit time. If one allows for the built-in field by adding a correction of V_{int}=0.40 V and V_{int}=0.30 V to the applied voltage for sample C and D, respectively, the currents prior to the transit of the charge carriers depend linearly on the total voltage $(V + V_{int})$. The various transients establish what has been termed an "envelope" curve [131], illustrated as the slow decreasing line in Fig. 7.5.

Such envelope curves indicate that transport is "ohmic" and for a given time t, the drift velocity of holes in μc-Si:H is proportional to the electric field (Note, that the normalized photocurrent has the dimensions of a mobility (cm^2/Vs)). The fact that even the 0 V transients agrees with the envelop curve indicates that the

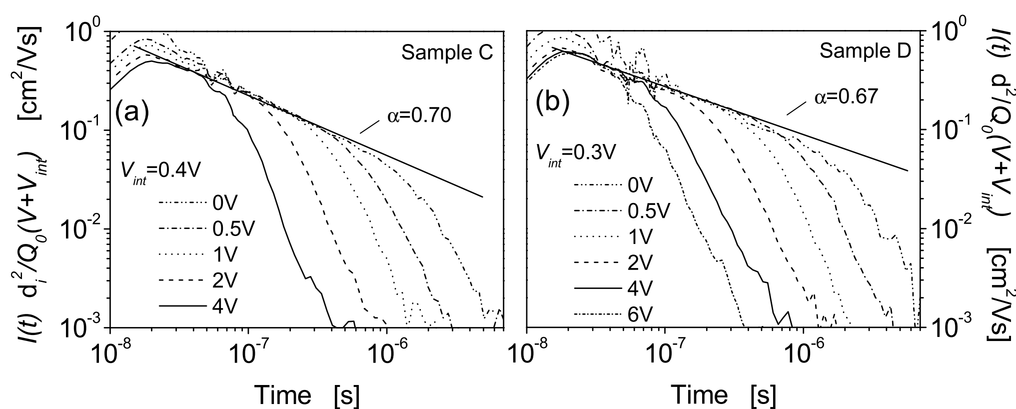

Figure 7.5: *Normalized transient photocurrents of (a) sample C and (b) sample D. The original, as measured, transients are shown in Fig. 7.3.*

assumption of an uniformly distributed internal field, made above, is valid. At this temperature, the envelope declines as a power-law ($t^{-1+\alpha}$) where α=0.70 and α=0.67 are the dispersion parameter for sample C and D, respectively. From the ”pretransit” regime the individual transits break at increasingly earlier times with increasing voltage. These breaks can be used to obtain a rough estimate of the transit times. For e.g. sample C the current transients exhibit ”transit times” varying from about 500 ns (for 0.5 V) to 70 ns (for 4V). For earlier times there is a noticeable increase of the photocurrent above this envelope, especially for the lower voltages. As already discussed above the absorption depth of the laser light was about 160 nm, which is about 5% of the sample thickness; electron motion is thus responsible for about 5% of the total photocharge. The excess current between 2×10^{-8} s and $6 \times 10^{-8} s$ is consistent with a rapid collection of this charge of electrons.

To summarize: Allowing to correct the externally applied voltage by a voltage due to the internal field the photocurrent transients show typical features expected for conventional time-of-flight interpretation. (i) Each transient can be divided in a ”pretransit” with shallow and ”posttransit” region with fairly steep power-law decay. (ii) The current transients exhibit ”transit times” increasing with decreasing applied electric field. (iii) The charge measurement for the high voltages approach the same asymptotic value for the total photocharge, indicating that Q_0 is likely a good estimate of the charge of photogenerated holes.

7.3 Temperature Dependent Drift Mobility

To get a closer insight into the processes determining the transport, transient photocurrents were measured in a range of temperatures between 125K and 300K. Fig. 7.6 displays, as an example, the transient photocurrent of sample C taken at V = 1V for several temperatures T in the range between 300K and 200K. The photocurrent transients show typical signs for temperature activated hole drift mobilities $\mu_{h,T}$. With decreasing temperature a declining magnitude of the current and a shift of the ”kink” to higher values can be observed. The photocharge transients $Q(t)$, determined by integrating the currents $I(t)$, approach the same asymptotic value for all temperatures. This indicates that the photogeneration quantum efficiency is independent of temperature and deep trapping is negligible in the measured temperature range. The dashed line in Fig. 7.6 (b) indicates the value of half the total collected photocharge $Q_0/2$. The times, where the photocharge transits cross this line can be interpreted as the time where half the charge has been collected (see section 3.1.4.3 for a detailed discussion). This value will be used as an estimate for the transit time t_τ used to calculate hole drift mobilities.

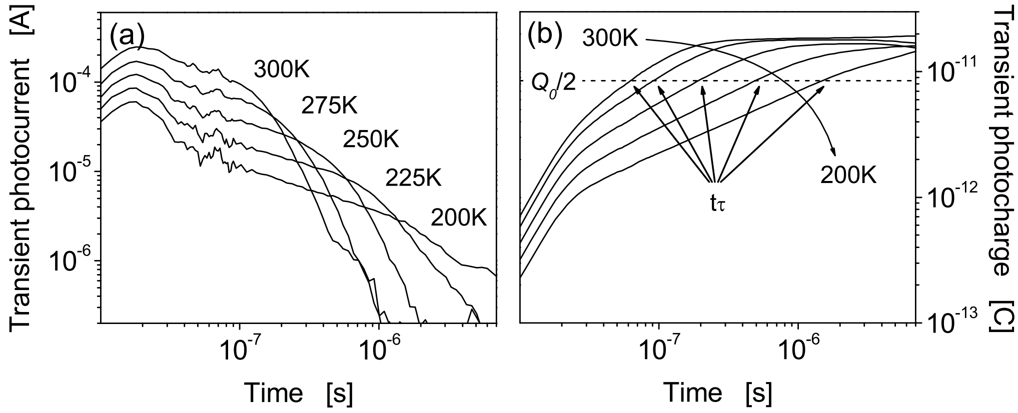

Figure 7.6: *(a) Temperature dependence of the transient photocurrent of sample C and (b) of the transient photocharge calculated by integrating the corresponding currents in panel (a).*

In Fig. 7.7 the temperature dependence for the average drift mobility of holes determined for sample C and D is illustrated. This average drift mobility is calculated as

$$\mu_{d,h} = \frac{L}{Ft_\tau} \tag{7.2}$$

where t_τ is the transit time for a particular ratio of a hole displacement L and the electric field F. Within this work

$$\frac{L}{F} = \frac{d^2}{2(V+V_{int})} = 7\times10^{-8}\ \mathrm{cm^2/V} \tag{7.3}$$

was used. Note, that for dispersive transport systems, drift mobilities for different materials must be compared at a specific value of L/F [131]. The straight line is a fit to the data of sample D, for which the measurement had the least scatter. However, sample C and D have essentially the same average hole drift mobility. The drift mobilities are simply activated with an activation energy of $E_A = 0.13$eV.

7.4 Multiple Trapping in Exponential Band-Tails

For sample C and D the model of multiple trapping in an exponential band-tail [100, 101, 98, 102, 103] was applied to the drift mobility data presented in section 7.2.2. The basic features of the model, which has been successfully applied to amorphous semiconductors, are discussed in section 2.4 and appendix A. In the multiple trapping model electronic states are simply divided into transport states (where the charge carriers are mobile) and traps, which simply immobilize the

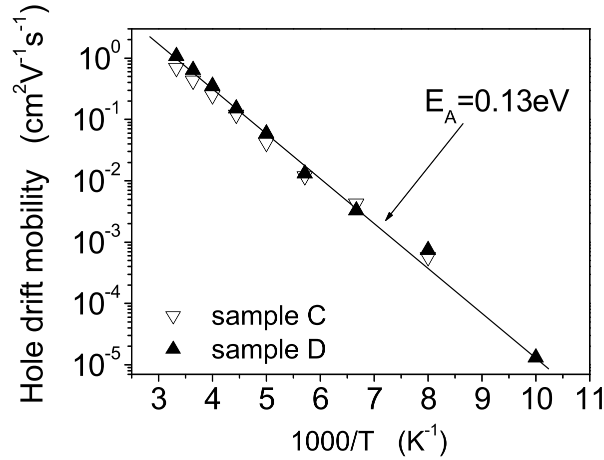

Figure 7.7: *Temperature dependence of the average hole drift mobility μ_D for samples C and D; μ_D was evaluated at a displacement/field ratio $L/F = 7\times10^{-8}cm^2/V$.*

charge carriers until they are thermally re-emitted into transport states. Although the physical mechanism of multiple trapping in exponential band-tails is rather complicated and involves a number of processes, the charge transport is mainly determined by the properties of the band-tail. In fact, the transport mechanism can be described by a set of only three parameters describing the band-tail. The model assumes a "band mobility" μ_0 for the holes. Measured drift mobilities are lower than this value because of the multiple-trapping of holes by localized states distributed as an exponential band-tail. The width of this band-tail, which lies just above the valence band edge, is denoted ΔE_V. The third parameter is the "attempt-to-escape" frequency ν, that characterizes thermal re-emission of holes from a band-tail trap back to the valence band. For fitting, the following function derived from the exponential band-tail model (see appendix A) was used:

$$\frac{L(t)}{F} = \frac{sin(\alpha\pi)}{\alpha\pi(1-\alpha)}\left(\frac{\mu_0}{\nu}\right)(\nu t)^{\alpha} \qquad \text{with} \qquad \alpha = \frac{kT}{\Delta E_V}. \tag{7.4}$$

Here $L(t)$ is the carrier displacement after a delay time t in an electric field F. In Fig. 7.8 the open symbols represent normalized transient photocharge measurements $Q(t)d^2/(Q_0(V + V_{int}))$ for several temperatures. It has been shown by Wang et al. [131], that for times prior t_τ ($t \ll t_\tau$) the normalized charge $(Q(t)d^2/(Q_0(V+V_{int})))$ equals $L(t)/F$. The physical meaning of the applied normalization is to consider the time t which is required for a carrier to be displaced by a distance L in an electric field F. The normalized photocharge transits have been recorded at bias voltages of $V = 0.5$ V and $V = 1$ V for specimen C and D, respectively, and were corrected by the internal voltage V_{int}. As already discussed,

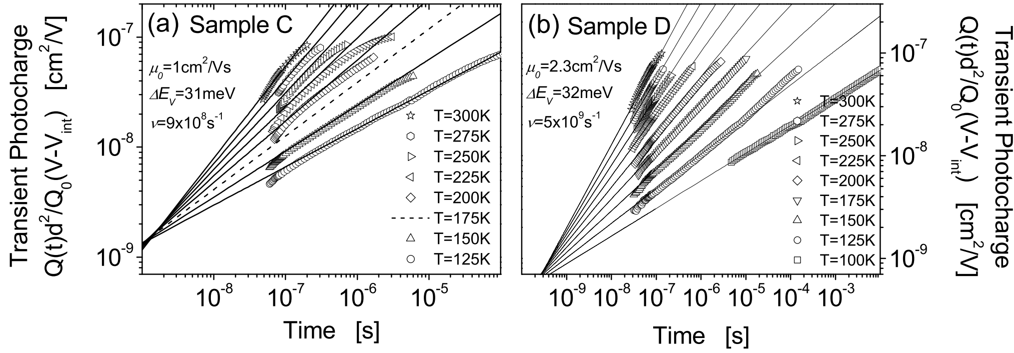

Figure 7.8: *Symbols are the normalized photocharge measurements taken on (a) sample C (V = 0.5 V) and (b) sample D (V = 1 V) at the indicated temperatures. The solid lines are the corresponding calculations using Eq. 7.4 with the parameters indicated.*

due to the absorption depth of the laser, which is 160 nm, about 5% of the charge is attributed to electron motion[1] and has been subtracted from the transient photocharge. The portions of these transients at early times close to the electronic rise-time ($t < 5 \times 10^{-8}$ s) have been excised, as have the late-time portions where most holes have been collected. The solid lines in Fig. 7.8 are a fit to the experimental measurements using the parameters listed in table 7.2. Additionally, the multiple trapping parameter of a typical a-Si:H sample taken from Dinca et al. [142] are shown. From the fitting a valence band-tail width of $\Delta E_V = 31$ meV for sample C ($\Delta E_V = 32$ meV for sample D) was derived, which is much narrower than the widths of $\Delta E_V = 40-50$ meV reported for amorphous silicon [140, 142], but is still substantially larger than the values as low as 22 meV that are reported for the conduction band-tail in amorphous silicon [131]. Remarkably, the values for the band mobility of $\mu_0 = 1$ cm^2/Vs for sample C and $\mu_0 = 2.3$ cm^2/Vs for D, are essentially the same as has been reported in amorphous silicon (for both electrons and holes) [131, 140, 142]. In this context it is interesting to note, that the attempt to escape frequency $\nu = 9 \times 10^8$ s^{-1} ($\nu = 5 \times 10^9$ s^{-1}) is approximately two to three orders of magnitude smaller than values that have been reported for holes in a-Si:H [140, 142].

7.5 Discussion

Transient photocurrent measurements have been performed on microcrystalline material prepared under plasma-deposition conditions similar to those where best solar cell performance can be achieved. As pointed out above, for conventional

[1]For a detailed discussion of the topic see section 3.1.4

Table 7.2: Multiple trapping fitting parameters

Multiple trapping Parameter	μc-Si:H sample C	μc-Si:H sample D	a-Si:H ref. [142]
Valence band mobility μ_0 [cm^2/Vs]	1.0	2.3	0.7
Band-tail width ΔE_V [meV]	31	32	45
Attempt-frequency ν [s^{-1}]	9×10^8	5×10^9	1×10^{12}

time-of-flight measurements, estimation of drift mobilities is best done in samples for which the depletion width d_w is close to the physical layer thickness d_i, which corresponds to a nearly uniform electric field across the intrinsic layer during the time-of-flight experiment. As can been seen in table 7.1 this criterion is not always fulfilled for the specimens investigated. In this section, the data of the samples where a standard time-of-flight analysis could be successfully applied will be summarized and discussed in more detail.

7.5.1 Photocurrent and Photocharge Transients

The photocurrent and photocharge transients presented in section 7.2.2 show several features expected for a conventional time-of-flight interpretation. First, the charge measurements for the higher voltages approach the same asymptotic value for the total photocharge Q_0. This indicates that Q_0 is likely a good estimate of the charge of photogenerated holes and that for the higher voltages no loss of photo-excited charge carriers occurs, e.g. due to deep trapping. Plotting the currents on a log-log scale, the photocurrent decays consist of two linear branches, indicating a power-law behavior typical for dispersive transport. Additionally, the current transients exhibit ”transit times” (where the power-law decay steepens markedly) varying from about 500 ns (for 0.5 V) to 70 ns (for 4 V). Even the 0 V transient has the form expected for time-of-flight, but does not have the correct asymptotic photo-charge. It seems reasonable that for 0V bias voltage applied the holes were ultimately trapped by deep levels (not band-tail states) during transit. Plotting the collected photocharge versus the voltages, a deep-trapping mobility-lifetime product for holes $\mu\tau_{h,t}$ of about 1×10^{-7} cm^{2}V could be evaluated. This value is in quite good agreement with earlier reports from Brueggemann et al. [23]; however, Juška and coworkers found a value which is about one magnitude lower than the one reported here [178]. These Hecht plots (see Fig. 7.4) have also been used to determine the internal field caused by the pin structure of the specimen. The obtained values of V_{int} = 0.3 V and 0.4 V are quite reasonable and expected for

a semiconductor device with a band gap of $E_G = 1.1$ eV. Considering the internal electric field, the normalized currents shown in Fig. 7.5 establish an "envelope" curve, indicating that, for a given time, the drift of holes depends linearly on electric field.

7.5.2 Hole Drift Mobilities

The drift mobilities have been evaluated using Eq. 3.9. At room temperature hole drift mobilities of $\mu_{d,h} \approx 1$ cm^2/Vs are obtained from these results. Additionally, temperature dependent photocurrent transients have been recorded in a range between 100K and 300K. The average drift mobility was evaluated at a particular "displacement/field" ratio of $L/F = 7 \times 10^{-8}$ cm^2/V. The hole drift mobilities derived are much larger than that of a-Si:H, where typical values are about two orders of magnitude smaller [142]. However, a direct experimental comparison at the same value for L/F is not possible, because the transit times t_τ in amorphous silicon expected for this L/F value would by far exceed the deep trapping life time τ_d. Thus, holes would already be captured by deep traps without any chance of release before they can reach the collecting electrode. Plotting $\mu_{d,h}$ in an Arrhenius plot shows that the hole drift mobility is simply activated with an activation energy of $E_A = 0.13$ eV. The physical meaning of E_A for multiple trapping in an exponential distribution of traps is still unclear. It has been suggested that E_A corresponds to an average energy required for a charge carrier trapped to release it above the mobility edge [100], but does not describe any particular feature, like a band-tail width or the depth of any particular trap.

Although electron and hole transport are crucial properties of these films, there are only few conclusive data regarding the drift mobilities of these carriers in μc-Si:H, and even less understanding of the physics governing carrier drift. The main experimental problem has been the high dark conductivity of many of the microcrystalline materials, which militates against conventional photocarrier time-of-flight estimation of drift mobilities. Mobility estimates have been reported using time-of-flight on specially compensated samples [143] and also using a novel "photo-CELIV" approach [179]. The results presented here differ qualitatively from these works performed on different samples of μc-Si:H, which found only a weak temperature-dependence [143, 179] and a strong electric-field dependence of the hole drift mobility [179]. The previous work differs from this both in samples measured and methods applied. However, recent work also performed on one sample prepared under conditions for optimized solar cells agrees in both the magnitude of the hole drift mobility and activation energy of $\mu_{d,h}$ [49].

7.5.3 The Meaning of Multiple Trapping

One approach to analyzing mobilities in polycrystalline materials is to invoke the effective masses, that would obtain for electrons and holes in the single crystal, and assume that the grain boundaries act as scatterers or barriers and as the locus for traps for the carriers [42]. It is instructive to use this approach crudely to calculate an "effective-mass carrier mobility" for holes $\mu_h^{e.m.}$ utilizing the expression $\mu_h^{e.m.} = \upsilon_{th} l/(kT/e)$, where υ_{th} is the "thermal velocity" for holes (about 10^7 cm/s in c-Si near room-temperature)[2] and l is a scattering length. If the scattering length is identified with a typical crystallite size of 3 nm, one infers $\mu_h^{e.m.} = 120$ cm^2/Vs, which is about 100 times larger than the estimate in Table 7.2. The effects of traps and barriers do not seem to explain the discrepancy for the samples, since these were already (implicitly) incorporated in the analysis that led to the estimate $\mu_0 = 1$ cm^2/Vs.

It is therefore most likely that the existence of band-tail states strongly effects the charge carrier transport. The disorder within the investigated material is sufficient to strongly alter the band edge states from their crystalline counterparts. In particular, a mobility-edge has been formed within the band-tail[3] (i.e. states lying deeper in the energy gap are localized).

The mobility-edge has been widely applied to amorphous semiconductors [97, 131], and has recently been applied to microcrystalline samples with a large fraction of amorphous "tissue" [73]. Here the suggestion is that it also applies to samples that are predominantly crystalline. In the mobility-edge model, hole states with energy levels below the mobility-edge ($E < E_V$) are completely delocalized (by definition), although with very different wave functions than the effective-mass states of crystals. Hole states lying above the mobility-edge ($E > E_V$) are localized. Both analytical and computational studies of mobility-edges [164, 180] indicate that the localization radius for a hole state grows very rapidly, and may even diverge, as the energy state approaches the mobility-edge. It is not clear theoretically how particular atomic-scale features such as "strained bonds" are incorporated into the band-tail states.

The estimates of 31 meV and 32 meV (see table 7.2) for the microcrystalline material seem unremarkable in the context of work on holes in amorphous silicon, which yields values in the range 40 – 50 meV. It is worth noting, that disorder affects holes and electrons very differently. The conduction band-tail in amorphous silicon has a width around 22 meV [97, 131]. Electron properties in samples quite

[2] The concept of a "thermal velocity" $\upsilon_{th} = (2k_BT/me)^{1/2}$ is based on effective-mass theory, and has no meaning in other transport models.

[3] The multiple-trapping model invokes a "transport edge" that most workers associate with Nevill Mott's "mobility-edge;" however, alternate views have been proposed, in particular "hopping only" and "potential fluctuation" models.

similar to the present ones have been studied using post-transit time-of-flight [73]. However the finding was that band-tail multiple-trapping did not apply for these transients. An interesting possibility is therefore that electron transport may be governed by effective masses in exactly the same material for which holes require a mobility-edge approach. The fact that the hole band-mobility μ_0 is about the same in the present microcrystalline samples and in amorphous silicon seems to support the mobility-edge interpretation, and more broadly suggests that a value near 1 cm^2/Vs may be a universal property of a mobility edge. Such "universality" is also suggested by the fact that electron band-mobilities in amorphous silicon are also around 1 cm^2/Vs [97, 131]. Interestingly, a band mobility of 1 cm^2/Vs is not an obvious implication of the existing theoretical treatments of mobility-edges.

It is quite interesting, that the value of the attempt-to-escape frequency for microcrystalline silicon is substantially (about 100 times) smaller than the lower values reported for a-Si:H. However, even for a-Si:H, there is no well-accepted physical interpretation for this parameter. One often-mentioned interpretation is that ν be identified as a "typical phonon frequency," but this association fails to explain either the very low magnitudes or the enormous range of magnitudes that have been reported experimentally [181, 182]. Yelon and Movaghar have suggested that multi-phonon effects lead to the variations and this perspective has been applied by Chen et al. to drift mobility measurements [183]. Another possibility originating with high-field drift mobility measurements in a-Si:H has been that ν reflects the bandedge density-of-states $g(E_V)$ [184], which suggests that the present measurements be interpreted as indicating a substantially lower value for $g(E_V)$ in microcrystalline than in amorphous silicon. Plainly, one needs more clues from experiment about the meaning of this parameter, however it seems possible that its dramatic lowering in microcrystalline silicon could be providing it.